Nanoscale

PAPER

View Article Online
View Journal | View Issue

Check for updates

Cite this: *Nanoscale*, 2023, **15**, 14165

Light-driven MOF-based micromotors with self-floating characteristics for water sterilization†

Hai Huang,‡[a] Yu Zhao,‡[a] Haowei Yang,‡[a] Jie Li,[a] Yulong Ying, *[a] Jinhua Li *[b] and Sheng Wang *[a]

Received 18th May 2023,
Accepted 28th July 2023

DOI: 10.1039/d3nr02299d

rsc.li/nanoscale

Three-dimensional motion (especially in the *Z*-axis direction) of metal–organic frameworks (MOFs)-based micromotors (MOFtors) is essential but still in its infancy. Herein, we propose a simple strategy for designing light-driven MOFtors that move in the *Z*-axis direction and efficiently kill *Staphylococcus aureus* (*S. aureus*). The as-prepared polypyrrole nanoparticles (PPy NPs) with excellent photothermal properties are combined with ZIF-8 through a simple *in situ* encapsulation method, resulting in multi-wavelength photothermally-responsive MOFtors (PPy/ZIF-8). Under the irradiation of near-infrared (NIR)/ultraviolet (UV)/blue light, the MOFtors all exhibited negative phototaxis and high-speed motion behaviour with the highest speed of 2215 ± 338 μm s^{-1}. In addition, it is proved that these MOFtors can slowly self-float up in an aqueous environment. The light irradiation will accelerate the upward movement of the MOFtors, and the time required for the MOFtors to move to the top is negatively correlated with the light intensity. Finally, efficient antibacterial performances (up to 98.89% against *S. aureus*) are achieved with these light-driven MOFtors owing to the boosted Zn^{2+} release by vigorous stirring motion and physical entrapment by the upward motion under light irradiation.

Introduction

Over the past decade, numerous exploratory studies on the three-dimensional (3D) motion (especially in the *Z*-axis direction) of micromotors have been proven critical for their potential applications in environmental remediation and biomedical fields.[1–3] Until now, micromotors based on traditional materials have been challenged by factors such as gravity settlement and insufficient driving force. Their motion mainly occurs at the bottom of the solution, that is two-dimensional (2D) movement with four degrees of freedom (4-DoF), which inhibits their further practical applications.[4–6] In the water purification field, it is difficult for micromotors with only 2D movement ability to perform efficient repair since the distribution of pollutants is random. It is found that the rapid movement of micromotors in the *Z*-axis direction can significantly promote liquid convection and favour the adsorption or degradation of pollutants. Specifically, microplastics, most of which are suspended in sewage, require the micromotors to grasp effectively through 3D motion with six degrees of freedom (6-DoF).[3] In light of the reported study,[7] the 3D random motion of micromotors can be realized simply by bubble recoil propulsion. Even though they can carry out high-speed motion thanks to the strong recoil force of the bubbles, the motion ability will gradually decay with the depletion of fuel until it stops moving, and the movement process is uncontrollable. Moreover, they are powered by toxic chemicals such as H_2O_2, N_2H_4, HCl, urea, and $NaBH_4$, which would be harmful to aquatic animals and plants.[8–12] Alternatively, a few studies have shown that the motion and control of micromotors in the *Z*-axis direction can be realized simultaneously by external fields (*e.g.*, a light field, an electric field, and the combination of a magnetic field and an acoustic field) without adding toxic chemicals.[2,13–18] The external field can supply energy to micromotors at any time, but the electric field or the combination of the magnetic and sound fields to trigger the *Z*-axis motion of micromotors have relatively higher requirements on external equipment and the operation is complicated and cumbersome, which causes another major limitation.

Light is a kind of environmentally-friendly energy with easy access and remote control characteristics. Light has been widely used as the driving source of micromotors benefiting from the high spatial-temporal precision and customization of many different parameters (such as light beam size, intensity,

---

[a] School of Materials Science and Engineering, Zhejiang Sci-Tech University, Hangzhou, 310018, China. E-mail: yingyulong@zstu.edu.cn, wangsheng571@hotmail.com

[b] School of Medical Technology, Beijing Institute of Technology, Beijing 100081, China. E-mail: lijinhua@bit.edu.cn

† Electronic supplementary information (ESI) available. See DOI: **https://doi.org/10.1039/d3nr02299d**

‡ These authors contributed equally to this work.

wavelength, incident angle, phase, and switch on/off).[19–25] Additionally, as a non-contact technique, light presents great versatility and flexibility in manipulating micromotors' motion behaviour (such as speed and trajectory).[26–30] Until now, only a few studies have been reported on the *Z*-axis motion of light-driven micromotors. Based on the intrinsic characteristics of photoactive materials or the interactions between light and matter, the *Z*-axis motion mechanism of light-driven micromotors can be divided into two types, *i.e.* photothermal conversion[2,13,31] and photochemical reactions.[3,14,32] Although some progress has been made, realizing the *Z*-axis motion of micromotors is still challenging.

In connection with the design of micromotors, the modulation of their weight and macro/microstructure is highly desired. Metal–organic frameworks (MOFs) are currently one of the most promising materials for preparing micromotors to perform their motion control in the *Z*-axis direction because their unique pore structure, large specific surface area, adjustable pore size, and controllable structure can effectively reduce the weight of micromotors and improve their motion ability in the *Z*-axis direction. Some MOFs have organic ligands with higher optical absorption coefficients than inorganic materials and metal sites with biomimetic catalytic activity, promoting the generation of light-induced gas or bubbles. MOFs have excellent gas adsorption properties, benefiting the adjustment of optically-controlled buoyancy in a liquid solution. The surface of MOFs is easily functionalized and can be modified with light-responsive polymers, aiming at regulating the hydrophilic/hydrophobic properties of light-driven MOFtors.[33,34] However, the development of MOFtors is slow. Based on the power sources, MOFtors are mainly propelled by the Marangoni effect, the bubble recoil effect based on Pt and H_2O_2, and an external magnetic field.[34] Particularly, to date, the study on light-driven MOFtors has been rarely reported. The existing MOFtors are also limited by the low design degree of freedom and poor motion ability in the *Z*-axis direction. Consequently, further investigations on the *Z*-axis motion of light-driven MOFtors are required to promote more potential applications (such as sterilizing and purifying environmental wastewater).

ZIF-8 is a kind of MOF synthesized by the reaction of Zn(II) and imidazole ligands, possessing many excellent properties and a wide range of practical applications.[35–37] Specifically, ZIF-8 and ZIF-8-based composites have demonstrated remarkable potential in antibacterial applications.[38–40] Previous studies have shown that ZIF-8 will partially hydrolyse in an aqueous environment, resulting in the release of Zn^{2+}.[41,42] Besides, light irradiation could accelerate the Zn^{2+} release rate.[43] Zn^{2+} is a potent antibacterial agent that can trigger cell deformation or cell wall rupture, resulting in cytoplasmic leakage and creating an alkaline microenvironment to inhibit the growth or kill bacteria.[44–46] Polypyrrole (PPy) is a conductive polymer widely used in the biomedical and environmental water treatment fields because of its fast response to light, excellent photothermal conversion performance, good hydrophobicity, outstanding biocompatibility, and stability.[47–49]

Herein, we demonstrate multi-wavelength photothermally-driven MOFtors, which move rapidly and serve as a micro-zone agitator, self-float in the *Z*-axis direction to the surface, and exhibit efficient antibacterial ability. The photothermally-responsive PPy NPs were incorporated into ZIF-8 *via* an *in situ* encapsulation method to obtain photothermally-driven MOFtors (PPy/ZIF-8). The effects of different wavelengths of light (*i.e.*, NIR/UV/blue light) on the motion behaviour of the MOFtors were studied. When the MOFtors were dispersed in water, the gas stored in the channel could transform into microbubbles due to their superhydrophobic properties, increasing their buoyancy and accounting for the slow self-floating phenomenon in the *Z*-axis direction. Furthermore, based on the photothermal PPy NPs, a light source was used to accelerate the extraction of the stored microbubbles, expand the bubble volume, and further increase the buoyancy of MOFtors. Cooperating with the liquid convection effect and enhanced self-floating ability of MOFtors in the *Z*-axis direction by photothermal action, many MOFtors accumulated on the top of the suspension, forming a dense MOFtor cluster. Finally, a superior antibacterial performance in simulated wastewater was achieved by these light-driven MOFtors attributed to the accelerated release of Zn^{2+}, boosted 3D stirring motion offering more contact possibility, and the entrapment effect of MOFtor clusters on bacteria during the ascent process.

Results and discussion

Preparation and characterization of PPy/ZIF-8 micromotors

A PPy/ZIF-8 micromotor was designed by a simple *in situ* encapsulation method. The detailed preparation process is shown in Fig. 1a. Spherical PPy NPs with an average size of 130 nm were prepared according to the reported method (Fig. 1b).[48] Then, the PPy NPs were introduced into the precursor solution for the synthesis of ZIF-8, in which sodium formate contributed to the deprotonation of 2-methylimidazole to coordinate with Zn^{2+} for quick ZIF-8 particle formation. The SEM and TEM results of the prepared PPy/ZIF-8 are illustrated in Fig. 1c–e, indicating the successful encapsulation of PPy NPs inside the ZIF-8 polyhedron. Compared with the unmodified pure ZIF-8 particles (Fig. S1†), the surface of PPy/ZIF-8 appeared wrinkled and rough, and a lot of PPy NPs could be observed on the surface, while the particle size did not change significantly, about 3 μm.

To study the crystal structure of PPy/ZIF-8, more detailed characterization experiments were performed. The X-ray diffraction (XRD) patterns showed that the main peaks of pure ZIF-8 were consistent with those of reported standard ZIF-8 crystals (Fig. 2a).[10] The strong diffraction peak of PPy/ZIF-8 was consistent with that of pure ZIF-8, and both of them had high crystallinity, indicating that the introduction of PPy NPs did not affect the crystal structure of ZIF-8. No additional peaks belonging to PPy NPs were observed due to the amorphous structure and low loading amount of PPy NPs.

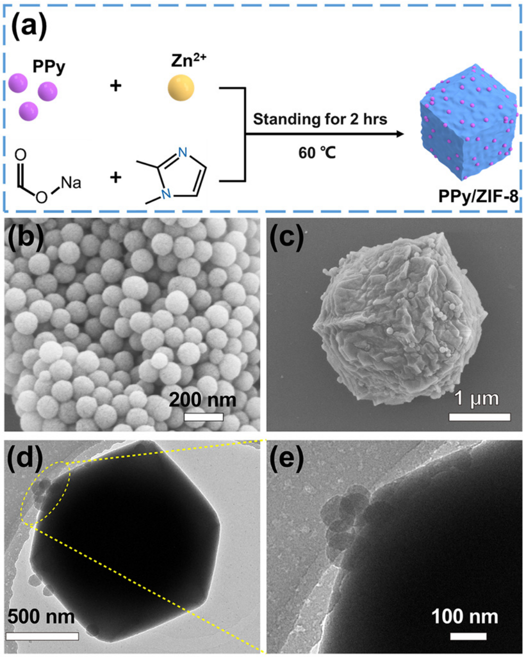

Fig. 1 Fabrication and morphological characterization. (a) Schematic illustrating the preparation of PPy/ZIF-8 through the *in situ* encapsulation method. SEM images of (b) PPy NPs and (c) PPy/ZIF-8. (d) TEM image of PPy/ZIF-8. (e) An enlarged view image of (d).

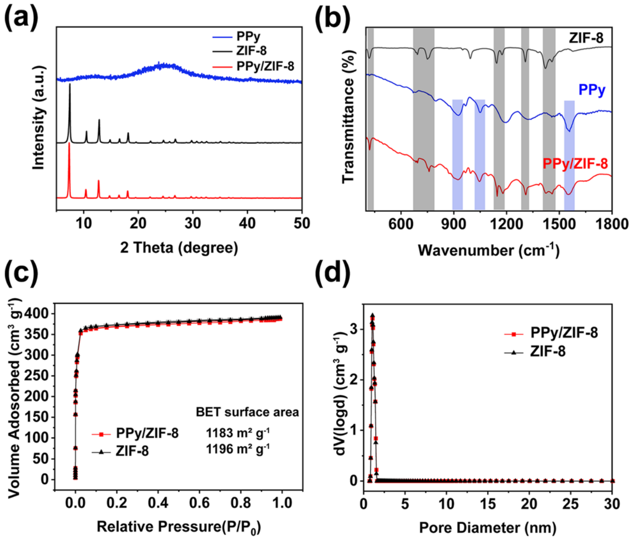

Fig. 2 Structural characterization. (a) Powder XRD patterns and (b) FTIR spectra of PPy NPs, ZIF-8, and PPy/ZIF-8. (c) N_2 adsorption–desorption isotherms and (d) pore size distributions of ZIF-8 and PPy/ZIF-8 based on the NLDFT method.

The composition of the PPy/ZIF-8 was further confirmed by Fourier transform infrared spectroscopy (FTIR) in Fig. 2b. PPy/ZIF-8 presented the typical characteristic peaks of ZIF-8 (marked in the grey column) at 692 cm^{-1} and 755 cm^{-1} (out-of-plane bending vibration of the imidazole ring); 1146 cm^{-1}, 1173 cm^{-1} and 1308 cm^{-1} (in-plane bending vibration of the imidazole ring); 1420 cm^{-1} and 1456 cm^{-1} (stretching vibration of the imidazole ring); and 420 cm^{-1} (stretching vibration of the Zn–N bond). The additional typical characteristic peaks of PPy (marked in the blue column) appeared at 1558 cm^{-1} (stretching vibration of the C=C bond, pyrrole ring stretching), 1048 cm^{-1} (in-plane deformation vibration of the C–H bond), and 927 cm^{-1} (out-of-plane bending vibration of the C–H bond). Additionally, the zeta potential of ZIF-8 was found to be 32.4 mV, while the value decreased to 22.2 mV for PPy/ZIF-8 (Fig. S2†). As the surface potential of PPy NPs is negative,[48] the presence of PPy NPs on the surface will lead to an overall potential decrease of ZIF-8.

The N_2 adsorption–desorption isotherms and pore size distributions of ZIF-8 and PPy/ZIF-8 at 77K are shown in Fig. 2c and d. ZIF-8 and PPy/ZIF-8 show type I isotherms with no desorption hysteresis, indicating the typical microporous structure. The calculated Brunauer–Emmett–Teller (BET) surface area of ZIF-8 and PPy/ZIF-8 was 1196 m^2 g^{-1} and 1183 m^2 g^{-1}, respectively. A nonlocal density functional theory (NLDFT) method was used to analyse the pore size distribution, confirming the existence of abundant micropores (<1.5 nm) in both ZIF-8 and PPy/ZIF-8 structures. The corresponding pore volumes were 0.531 cm^3 g^{-1} and 0.527 cm^3 g^{-1}, respectively. The above results indicated that the introduction of PPy NPs into the ZIF-8 structure by the *in situ* encapsulation method hardly affects the specific surface area and blocks the inherent micropore structure of ZIF-8.

Motion behavior of the light-driven PPy/ZIF-8 micromotors

The as-prepared PPy/ZIF-8 particles only exhibited Brownian motion without light irradiation (Mov. S1†). When exposed to blue light (470 nm), the PPy/ZIF-8 micromotors exhibited negative phototaxis, *i.e.*, spread from the centre of the blue light spot to the surrounding area (Fig. 3a and Mov. S2†). Besides, we also characterized the motion behaviour of the PPy/ZIF-8 micromotors at other different wavelengths of light (808 nm and 365 nm). At the same light intensity of 0.6 W cm^{-2} in Fig. 3b and Mov. S2,† the micromotors showed a high-speed motion of negative phototaxis under all three types of light at an average speed of 2215 ± 338 μm s^{-1} (NIR light), 1301 ± 203 μm s^{-1} (UV light), and 780 ± 161 μm s^{-1} (blue light), respectively. In contrast, the pure ZIF-8 particles maintained the Brownian motion state in the presence or absence of the three kinds of light irradiation (Mov. S3†). It is indicated that the encapsulation of PPy NPs significantly improved the motility of the micromotors. Once the light source was turned off, the micromotors would gradually stop the light-induced motion and resumed Brownian motion. As illustrated in Fig. 3c, the speed of the light-driven micromotors can be modulated on demand by adjusting the light intensity. When the blue light intensity increased from 0.1 to 0.6 W cm^{-2}, the average speed of the micromotors increased significantly from 80 ± 19 to 780 ± 161 μm s^{-1}. These results demonstrate that the motion behaviour and "on–off" movement of the PPy/ZIF-8 micromotors can be controlled by the light source of different wavelengths and intensities.

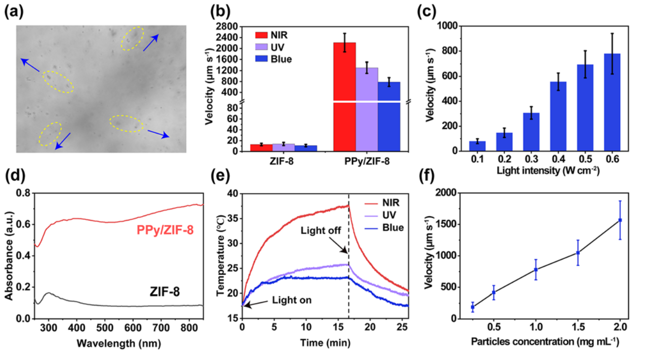

Fig. 3 Motion behaviour of light-driven PPy/ZIF-8 micromotors. (a) The motion of PPy/ZIF-8 micromotors away from the centre of the blue light spot (image was extracted from Mov. S2,† the direction of motion is indicated by the blue arrows). (b) Motion speeds of ZIF-8 and PPy/ZIF-8 (1 mg mL^{-1}) under the irradiation of NIR, UV, and blue light (0.6 W cm^{-2}), respectively. (c) Motion speed of PPy/ZIF-8 micromotors under different intensities of blue light irradiation (1 mg mL^{-1}). (d) UV-vis-NIR spectra of ZIF-8 and PPy/ZIF-8. (e) Change of the temperature of PPy/ZIF-8 suspension (1 mg mL^{-1}) with time under NIR, UV, and blue light irradiation (0.6 W cm^{-2}), respectively. (f) Effect of PPy/ZIF-8 micromotor concentration on the motion speed under blue light irradiation (0.6 W cm^{-2}). The error bars indicate the standard deviation (n = 3; mean ± s.d.).

Notably, PPy NPs have a wide light absorption band and excellent photothermal conversion performance.[50] Therefore, compared with the pure ZIF-8 particles, PPy/ZIF-8 micromotors exhibited a stronger light absorption capacity and a broader NIR absorption band (Fig. 3d), which can quickly and efficiently convert light energy into thermal energy, thus triggering the negative phototaxis movement caused by the photothermal effect. As shown in Fig. 3e, the temperature of the suspension containing micromotors increased sharply within the first 10 min exposure to NIR light and then gradually slowed down when the light turned off. When irradiated with UV or blue light, the suspension temperature increased rapidly within the first 3 min and then remained unchanged. The photothermal conversion efficiency of UV light is higher than that of blue light, but both are much lower than that of NIR light. The above results show that the photothermal conversion ability of the micromotors is highly dependent on the wavelength of light and determines the motion ability (Fig. 3b and d). Hence, the distinct NIR adsorption and photothermal conversion ability of PPy is crucial for triggering the fastest speed of the micromotors under NIR light irradiation in our study. Given the widely accepted mechanism that the concentration of photothermally active particles is positively correlated with the heat generated by light irradiation,[2,51] we also investigated the effect of the concentration of the micromotors on the light-driven speed, as shown in Fig. 3f. Under the irradiation of blue light, the motion speed of the micromotors increased almost linearly with the concentration of micromotors. Additionally, the motion of photothermal micromotors can be triggered by the asymmetric thermal effect or the natural convection of fluids.[52,53] For the PPy/ZIF-8 micromotors we designed here, they moved from a hot irradiated area to a cold unirradiated area, which is consistent with the classic reported studies of self-thermophoretic motion.[54,55] All the above results demonstrated that the photothermal effect of PPy NPs powered the negative phototactic motion of micromotors.

Z-axis motion of the PPy/ZIF-8 micromotors

PPy/ZIF-8 micromotors not only exhibited a negative phototaxis but also had the ability to slowly self-float up without light exposure. Fig. 4a shows how the suspension containing micromotors changes from opaque to transparent over time, *i.e.*, the micromotors eventually aggregate on the top of the suspension to form dense black clusters due to the self-floating. Specifically, the suspension was cloudy and opaque when initially added to the cuvette, and the micromotors would slowly self-float up under static treatment (Fig. 4a1). After 20 min, a few micromotors were observed floating up to the top of the suspension (Fig. 4a2). Subsequently, the self-floating of micromotors will continue. After 2 h, it was observed that many micromotors had floated to the top of the suspension, and some were floating (Fig. 4a3). It was worth noting that the continuous generation of many tiny bubbles was observed throughout the self-floating process.

Based on the negative phototactic motion of the micromotors triggered by the photothermal effect under three types of light irradiation, the effect of illumination on the *Z*-axis motion was studied, as shown in Fig. 4b. Herein, blue light was selected as the light source and came from the bottom of the cuvette to trigger the *Z*-axis motion of the micromotors. As presented in Fig. 4b1, the suspension was initially in an

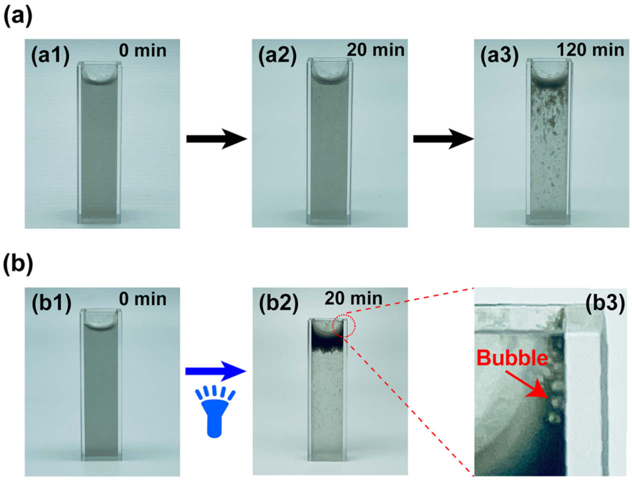

Fig. 4 *Z*-axis motion of PPy/ZIF-8 micromotors. (a) Slow self-floating of PPy/ZIF-8 micromotors (1.5 mg mL^{-1}) under static conditions; (a1–a3) optical images illustrating the suspension state at 0, 20, and 120 min. (b) Incident blue light (0.6 W cm^{-2}) from the bottom of the suspension to accelerate the *Z*-axis movement of PPy/ZIF-8 micromotors (1.5 mg mL^{-1}); (b1 and b2) optical images illustrating the suspension state at 0 and 20 min during blue light irradiation; (b3) an enlarged image of (b2) showing the formation of bubbles.

opaque state similar to Fig. 4a1. Then, under light irradiation, the micromotors would move rapidly in the *Z*-axis direction, playing a role of micro-stirring and producing more bubbles throughout the process. After 20 min blue light irradiation, almost all the micromotors moved to the top of the suspension, forming a thick black layer of micromotor clusters (Fig. 4b2). Simultaneously, many large bubbles can be clearly observed at the edge of the top of the cuvette (as shown in Fig. 4b3, marked by the red arrow). Additionally, the time required for the micromotors to move to the top of the suspension entirely is inversely proportional to the light intensity, indicating that the *Z*-axis movement capability of the micromotors can be controlled by modulation of the light intensity (Fig. S3†).

In addition, we pipetted the suspensions at the top of the cuvette at 0 and 20 min during the blue light irradiation and characterized them under an optical microscope, respectively. As illustrated in Fig. 5a and b, it is evident that there were only a small number of micromotors at the top of the suspension prior to illumination. In contrast, PPy/ZIF-8 micromotors gathered at the top and arranged closely after 20 min of blue light irradiation. Therefore, we concluded that the micromotors could move in the *Z*-axis direction with or without light irradiation and eventually float on the top of the suspension for a long time. Moreover, light irradiation could accelerate the movement of the micromotors in the *Z*-axis. In our view, the reasons for the above phenomenon are the following: as shown in Fig. 5c, pure ZIF-8 had a water contact angle of 96.3 ± 1.1°, while the water contact angle of the PPy/ZIF-8 micromotor increased to 150.0 ± 1.5°, *i.e.*, superhydrophobicity (Fig. 5d). The PPy/ZIF-8 micromotors had a large number of pores and channels inherent to ZIF-8. In the absence of light irradiation, when the micromotor was dispersed in water, a stable solid–liquid–gas three-phase interface would be generated at the microporous structure due to its superhydrophobicity. Along with the time, the stored gas limited inside the micromotor transformed into microbubbles, increased the buoyancy of the micromotor against gravity, and led to the micromotors float up spontaneously. When the blue light came from the bottom of the cuvette, the micromotors converted the absorbed light energy into heat energy, expanding a large number of stored microbubbles and further increasing the buoyancy of the micromotor. Additionally, the micromotors acted as a heat source. A temperature gradient was produced between the illuminated and non-illuminated areas upon blue light exposure, resulting in strong liquid convection between cold and hot solvent molecules (that is, the ultrafast motion observed in microscopy). Hence, the rapid stirring and upward motion of the micromotor in the *Z*-axis direction are determined by the heat transfer between the hot and cold solvent molecules and the increased buoyancy due to the thermally induced rapid expansion of the stored microbubbles.

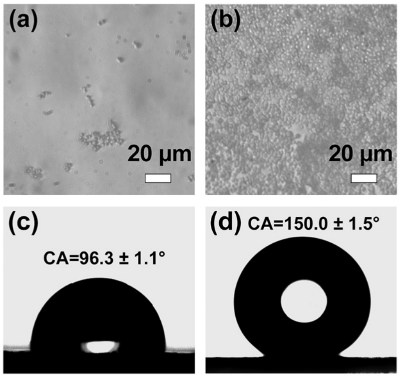

Fig. 5 Optical microscopy images of the top suspension (both pipetting 20 μL) of the light irradiation group at (a) 0 min and (b) 20 min (corresponding to Fig. 4b1 and b2, respectively). Water contact angles of (c) pure ZIF-8 and (d) PPy/ZIF-8 micromotors.

Antibacterial performances of the PPy/ZIF-8 micromotor in water sterilization

Staphylococcus aureus (*S. aureus*), commonly found in wastewater, was selected as the bacteria model to test the antibacterial performance of ZIF-8 and PPy/ZIF-8 micromotors in aqueous environments. As shown in Fig. 6a, the colony forming unit (CFU) counting method was used to quantitatively analyse the antibacterial effectiveness with different treatments, and the corresponding results are shown in Fig. 6b. Specifically, *S. aureus* treated with sterile water as the control group showed a very low antibacterial rate under both light irradiation and dark room standing conditions. It was found that a small amount of PPy/ZIF-8 micromotors self-floated to the top of the suspension in the dark room static treatment group, while ZIF-8 did not exhibit a self-floating phenomenon. The corresponding antibacterial rates were 27.49% and 23.17%, respectively. However, under light irradiation, the PPy/ZIF-8 micromotors showed rapid stirring motion in the *Z*-axis direction and eventually moved to the top of the suspension, while the motion of ZIF-8 was not observed. The corresponding antibacterial rates were increased to 98.89% and 66.73%, respectively. The above experimental results indicated that the rapid stirring and upward motion of PPy/ZIF-8 micromotors triggered by the photothermal effect further enhances the antibacterial performance of PPy/ZIF-8 micromotors.

ZIF-8 is unstable in aqueous environments, releasing Zn^{2+} into the aqueous solution, and its decomposition rate would be accelerated by light irradiation:[41–44]

$$\mathrm{Zn(mIm)_2 + 2H_2O \leftrightarrow Zn^{2+} + 2HmIm + 2OH^-}.$$

Besides, Zn^{2+} had been widely proven as a highly desirable antibacterial agent,[45,46,56] which could induce cell deformation or cell wall rupture, resulting in cytoplasmic leakage and the creation of an alkaline microenvironment, thereby achieving the purpose of growth inhibition or death of the bacteria.

To clarify the spontaneous disintegration behaviour of ZIF-8 and PPy/ZIF-8 micromotors in an aqueous environment and the underlying antibacterial mechanism, the Zn^{2+} concen-

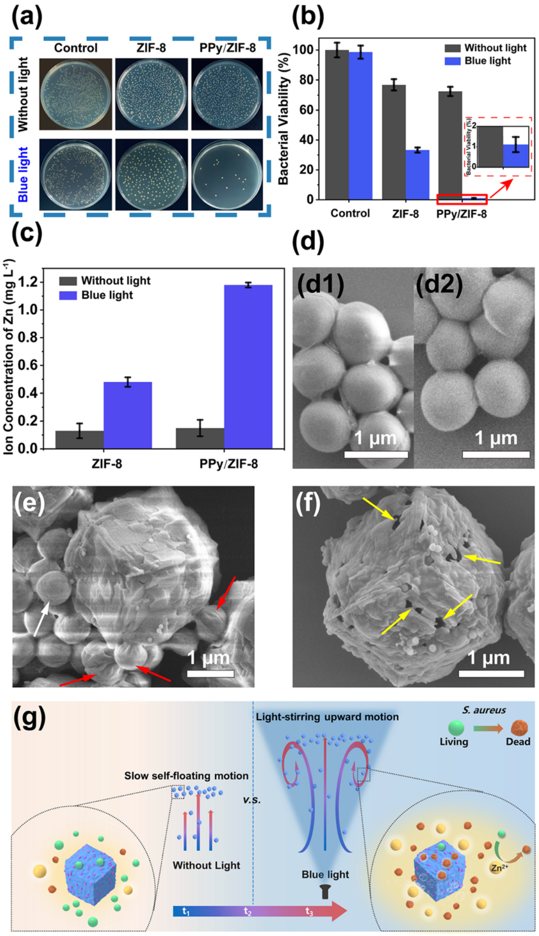

Fig. 6 Antibacterial performance of PPy/ZIF-8 micromotors. (a) Plate photographs of *S. aureus* with sterile water, ZIF-8, and PPy/ZIF-8 treatments under blue light irradiation/dark room standing conditions and (b) the corresponding bacterial viabilities. (c) Zn^{2+} concentration of the supernatant solution of ZIF-8 and PPy/ZIF-8 micromotors under blue light irradiation/dark room standing conditions. SEM images under different treatment conditions in the antibacterial experiment: *S. aureus* after sterile water treatment under (d1) blue light irradiation and (d2) dark room standing conditions; (e) the top of the suspension treated with PPy/ZIF-8 micromotors (live/dead *S. aureus* cells marked by the white/red arrows, respectively); and (f) the PPy/ZIF-8 micromotor with a partially decomposed surface (broken holes marked by the yellow arrows) under blue light irradiation. All the above blue light was used with an intensity of 0.3 W cm^{-2}, and the dark room standing treatment time was 30 min. The error bars indicate the standard deviation ($n = 3$; mean ± s.d.). (g) Schematic diagram illustrating the motion and antibacterial mechanism along with time from t_1 to t_3.

tration in the aqueous solution under light irradiation/dark room standing conditions was characterized, and the corresponding SEM images related to antimicrobial experiments were recorded. The release amount of Zn^{2+} is provided in Fig. 6c. Under dark room standing conditions, the released amount of Zn^{2+} from ZIF-8 and PPy/ZIF-8 micromotors was 0.13 and 0.15 mg L^{-1}, respectively, indicating that ZIF-8 and PPy/ZIF-8 micromotors released roughly the same amount of Zn^{2+}. Nevertheless, the PPy/ZIF-8 micromotors (27.49%) showed slightly stronger antibacterial ability than ZIF-8 (23.17%), which may be due to the fact that the PPy/ZIF-8 micromotors entrained a small amount of bacteria during the self-floating process. However, under light irradiation, the release amount of Zn^{2+} from the PPy/ZIF-8 micromotors significantly increased from 0.48 mg L^{-1} to 1.18 mg L^{-1}, but the amount of Zn^{2+} released from ZIF-8 remained basically unchanged. The different release amounts of Zn^{2+} were mainly attributed to the light-boosted self-decomposition and the rapid motion of the PPy/ZIF-8 micromotors triggered by the photothermal effect. Meanwhile, the antibacterial ability of PPy/ZIF-8 micromotors (98.89%) was much stronger than that of ZIF-8 (66.73%), owing to the synergistic antibacterial effect by the rapid stirring and *Z*-axis motion of PPy/ZIF-8 micromotors, *i.e.*, the release of a large amount of Zn^{2+} and the entrapment of some bacteria. As illustrated in Fig. 6d, the *S. aureus* cells treated with sterile water were plump, and the surface was smooth under light irradiation/dark room standing conditions, indicating that their activity was unaffected. Significantly, as shown in Fig. 6e, the SEM images of the top suspension after the antibacterial process using the PPy/ZIF-8 micromotors under blue light irradiation showed that the surface of most *S. aureus* cells was sunken and wrinkled (marked by the red arrows), indicating the damage of cell structure and the loss of metabolism. Only a few *S. aureus* cells had typical structures and maintained the original active state (marked by the white arrow). Notably, as illustrated in Fig. 6f, the partial PPy/ZIF-8 micromotors presented a surface with damaged holes, demonstrating the accelerated release of Zn^{2+} under light irradiation. Thus, the light-driven PPy/ZIF-8 micromotors exhibited excellent antibacterial abilities mainly due to the promoted Zn^{2+} release by the incident light, light-induced stirring movement, and a particular synergistic antibacterial effect where some bacteria were physically entrapped during the ascending motion of the micromotors (Fig. 6g).

Conclusion

In summary, PPy/ZIF-8 micromotors with a multi-wavelength light response and excellent antibacterial abilities were prepared through a simple *in situ* encapsulation method. ZIF-8 microparticles and PPy/ZIF-8 micromotors only exhibited simple Brownian motion without light irradiation. When exposed to three different wavelengths of light sources, the ZIF-8 particles maintained the Brownian motion state. In contrast, the PPy/ZIF-8 micromotors exhibited rapid negative phototaxis motion at average speeds of 2215 ± 338 μm s^{-1} (NIR light), 1301 ± 203 μm s^{-1} (UV light), and 780 ± 161 μm s^{-1} (blue light), respectively, indicating the crucial role of PPy NPs in the movement. A series of experiments proved that the photothermal ability of micromotors is highly dependent on the wavelength of light, determining the subsequent motion ability. The concentration of micromotors has a positive linear effect on the motion velocity. Besides, the PPy/

ZIF-8 micromotors exhibited the self-floating ability due to the inherent superhydrophobic properties with the encapsulation of PPy, resulting in the buoyancy increase when the micromotors were dispersed in water, where the stored gas could transform into bubbles. Under light irradiation, the rising temperature could accelerate this process, resulting in a faster upward motion to the surface of the suspension. The micromotors exhibited a strong antibacterial ability of 98.89% as an antibacterial agent against the common bacteria (*S. aureus*) in wastewater within 30 min, mainly due to the synergistic effect under light irradiation, *i.e.*, the boosting release of Zn^{2+} by light, the light-induced fast stirring motion, and the physical entrapment during the ascending motion. Our study enlightens the significance for the future design of light-driven 3D-motion MOFtors and provides an effective solution for potential wastewater sterilization.

Experimental

Chemicals

Iron chloride hexahydrate ($FeCl_3 \cdot 6H_2O$, 99%), pyrrole (Py, 99%), sodium formate (HCOONa, 99.5%), and 2-methylimidazole ($C_4H_6N_2$, 99%) were purchased from Shanghai Macklin Reagent Co., Ltd. Poly(vinyl alcohol) (PVA, $M_w \sim 31\,000$) and zinc nitrate hexahydrate ($Zn(NO_3)_2 \cdot 6H_2O$, 99%) were purchased from Aladdin Industrial Corporation. Ethanol (CH_3CH_2OH, ≥99.9%) and methanol (CH_3OH, ≥99.9%) were purchased from Hangzhou Gaojing Fine Chemical Industry Co., Ltd. All chemical reagents were used without further purification. Ultrapure deionized water (18.2 MΩ cm) was used throughout all the experiments.

Preparation of PPy NPs

PPy NPs were prepared following a previously reported method.[48] Briefly, 1.5 g of PVA was added to 20 mL of deionized water. Then the solution was placed in a thermostatic water bath at 60 °C with a magnetic stir bar until the PVA completely dissolved, followed by cooling to room temperature. Then 1.2434 g of $FeCl_3 \cdot 6H_2O$ was dissolved in the mixture by magnetic stirring at room temperature for 1 h. After another 1 h to allow equilibration, 140 μL of Py solution was added dropwise into the aqueous PVA/$FeCl_3$ solution. Then the mixture was transferred to a low-temperature reaction tank, and the polymerization was performed under magnetic stirring at 5 °C for 24 h. The resulting product was separated from the dispersion solution by centrifugation and washed three times with deionized water to remove impurities. A black PPy NP powder was obtained by drying the precipitate in a vacuum oven at room temperature for 12 h.

Preparation of PPy/ZIF-8 micromotors and ZIF-8

For the preparation of PPy/ZIF-8 micromotors, an *in situ* encapsulation method was used. Concisely, 8 mg of the as-obtained PPy NPs were added to 20 mL of deionized water and dispersed by ultrasonic treatment at room temperature for 3 h, and then 0.29 g of $Zn(NO_3)_2 \cdot 6H_2O$ was dissolved in the mixture by ultrasonic treatment for 20 s to obtain mixed solution A. 2.27 g of 2-methylimidazole and 0.269 g of sodium formate were added to another 20 mL of deionized water. Mixed solution B was obtained by ultrasonically dispersing the mixture at room temperature for 2 min. Afterwards, the above solutions of A and B were mixed and homogenized by ultrasound for 5 min and then stood at 60 °C for 2 h. The precipitate was collected by centrifugation, washed twice with ethanol and methanol to remove the remaining reactants, and dried in a vacuum oven for 12 h to obtain a dark grey PPy/ZIF-8 powder.

The preparation of ZIF-8 is similar to the method of synthesizing PPy/ZIF-8. The only difference is that PPy NPs were not added during the synthesis.

Characterization

The morphologies of the particles were captured by using field-emission scanning electron microscopy (FESEM, Hitachi S-4800, Japan). Transmission electron microscopy (TEM) images were recorded using a JEM-2100. Powder X-ray diffraction (XRD) patterns were obtained using a Bruker Focus D8 Phaser system with a Cu Kα radiation of 1.54178 Å, operating at 40 kV and 40 mA. The infrared spectrum of the as-synthesized particles was recorded using a Fourier transform infrared spectrometer (FTIR, Nicolet 6700). Nitrogen adsorption studies were performed with a Quantachrome Autosorb IQ3 analyzer at 77 K after the two samples were degassed at 120 °C for 8 h. Pore size distribution data were obtained using a nonlocal density functional theory (NLDFT) model. Zeta potentials were measured in water at pH 7 using a Malvern Zetasizer Nano ZS90. Absorbance spectra of the samples were recorded using a UH4150 UV/Vis/NIR spectrometer. The temperature changes of the PPy/ZIF-8 suspension were recorded using an infrared thermometer. Contact angle measurement was performed on a Dataphysics OCA 25 instrument.

Light-driven motion record and analysis

The powders of ZIF-8 and PPy/ZIF-8 were dispersed in deionized water before the test, respectively. 100 μL of suspension containing samples of different concentrations was dropped onto a glass slide. The light irradiation provided by an external point light source illuminator, including NIR (808 nm)/blue (470 nm)/UV (365 nm) light, was used to excite the motion. An inverted optical microscope (ICX41-FLEDT, Ningbo Sunny Instruments Co., Ltd.) coupled with a 20x objective was used for observation and video recording. The light intensity was measured using a Thorlabs PM100USB optical power density meter. Unless otherwise stated, the intensity of the light source driving the sample was 0.6 W cm^{-2}. Videos with a typical length of 10 s were taken using a Point Grey camera (BFS-U331S4M-C) mounted on the microscope at a frame rate of 20 per second (20 fps), and the motion was analysed using the free MTrackJ plugin in the ImageJ program. The average speed calculated in this work is the motion speed on the *XY* planes, *i.e.*, V_{xy}, due to the difficulty in the motion measurement in the *Z* direction (Fig. S4†). The average speed was calculated from more than 60 MOFtors under every condition, and the error bar was presented using the standard error of the mean.

Each suspension containing 3.8 mL of PPy/ZIF-8 (1.5 mg mL^{-1}) was added to two fully transparent cuvettes (4.5 mL) to explore the *Z*-axis motion of the PPy/ZIF-8 micromotors on the macro scale. One group was irradiated with blue light (0.6 W cm^{-2}) from the bottom of the cuvette, and the other group was left standing in a dark room without light. After 20 min, the light was removed to observe the evolution of the two groups of suspensions. 20 μL of the suspension at the top of the light group was pipetted at 0 min and 20 min, respectively, and placed under an optical microscope to evaluate the number of micromotors. The relationship between the light intensity and the time required for the PPy/ZIF-8 micromotors (1.5 mg mL^{-1}) completely floating to the top of the suspension was studied.

Antibacterial performance tests

Staphylococcus aureus (*S.aureus*), a common bacterium in wastewater, was selected as the target model bacteria to evaluate the antibacterial performance of the PPy/ZIF-8 micromotor. The bacterial strains were incubated with shaking in Luria–Bertani (LB) liquid medium at 37 °C. Each 260 μL of bacteria (the concentration was 10^5 CFU mL^{-1}) diluted with sterile water was added to four cuvettes of 3.8 mL of suspensions containing ZIF-8 or PPy/ZIF-8 (the final concentration was 0.38 mg mL^{-1}) for the antibacterial test. Specific tests were performed under four conditions: (1) standing in a dark room, ZIF-8 + bacteria; (2) light irradiation, ZIF-8 + bacteria; (3) standing in a dark room, PPy/ZIF-8 + bacteria; (4) light irradiation, PPy/ZIF-8 + bacteria. The above illumination treatment refers to irradiating with blue light (0.3 W cm^{-2}) from the bottom of the cuvette. After the antibacterial process for 30 min, 20 μL of suspensions near the bottom of the cuvette were dipped on an LB agar plate and incubated at 37 °C for 24 h. The viability of bacteria was quantitatively analyzed by the colony forming unit (CFU) counting method.

To identify the antibacterial performance of the four conditions, two sets of control experiments were carried out under the above same experimental conditions: the difference is that the suspension containing antibacterial agents (ZIF-8 or PPy/ZIF-8) was replaced with an equal volume (3.8 mL) of sterile water, and treated in a dark room or light irradiation for 30 min. All the data of bacterial viability were determined from three parallel experiments and expressed as the mean ± standard deviation.

Zinc ion (Zn^{2+}) release test

To study the release amount of Zn^{2+} from ZIF-8 or PPy/ZIF-8 under light irradiation/dark room conditions, the above four groups of suspensions containing ZIF-8 or PPy/ZIF-8 were prepared and treated with standing in a dark room or light irradiation (blue light, 0.3 W cm^{-2}) for 30 min, respectively. Then, the supernatant of each group was collected by centrifugation, and the contents of Zn^{2+} in the supernatant were measured by ICP-MS (iCAP Qc, ThermoFisher Scientific).

Observation of the bacterial morphology

SEM was used to observe the changes in the bacterial morphology of the antibacterial agents. The collected suspension containing bacteria was fixed overnight with a 2.5% glutaraldehyde stationary solution at 4 °C. Ethanol with concentrations of 30%, 50%, 70%, 90% and 100% (15 min each) was used to dehydrate the samples containing bacteria sequentially. Eventually, the samples were sputtered with platinum coating for SEM images.

Author contributions

H. Huang conducted the preparation and characterization. Y. Zhao and H. W. Yang performed the motion tracking and analysis. H. Huang, Y. Zhao, and H. W. Yang together wrote the draft of the manuscript. J. Li conducted part of the materials preparation. S. Wang helped in performing the project with constructive discussions. J. H. Li helped in carrying out the *in vitro* antibacterial experiments. Y. L. Ying supervised the research and initiated the research line. All authors discussed the results and contributed to the manuscript writing.

Conflicts of interest

There are no conflicts to declare.

Acknowledgements

H. Huang, Y. Zhao, H. W. Yang, J. Li, and Y. L. Ying were supported by the National Natural Science Foundation of China (52203147), the Zhejiang Provincial Natural Science Foundation of China (LQ22B010006), and the Science Foundation of Zhejiang Sci-Tech University (21212243-Y). J. H. Li sincerely acknowledges the financial support from the Beijing Institute of Technology Teli Young Fellow Program (RCPT-20220029). S. Wang was supported by the Zhejiang Provincial Natural Science Foundation of China (LZ22C100002).

References

1 Z. Guo, T. Wang, A. Rawal, J. Hou, Z. Cao, H. Zhang, J. Xu, Z. Gu, V. Chen and K. Liang, *Mater. Today*, 2019, **28**, 10–16.
2 Y. Hu, W. Liu and Y. Sun, *ACS Appl. Mater. Interfaces*, 2020, **12**, 41495–41505.
3 M. Urso, M. Ussia, F. Novotný and M. Pumera, *Nat. Commun.*, 2022, **13**, 3573.

4 M. Fernández-Medina, M. A. Ramos-Docampo, O. Hovorka, V. Salgueiriño and B. Städler, *Adv. Funct. Mater.*, 2020, **30**, 1908283.

5 A. D. Fusi, Y. Li, A. Llopis-Lorente, T. Patiño, J. C. M. van Hest and L. K. E. A. Abdelmohsen, *Angew. Chem., Int. Ed.*, 2023, **62**, e202214754.

6 T. Xu, L.-P. Xu and X. Zhang, *Appl. Mater. Today*, 2017, **9**, 493–503.

7 Y. Yang, X. Arqué, T. Patiño, V. Guillerm, P.-R. Blersch, J. Pérez-Carvajal, I. Imaz, D. Maspoch and S. Sánchez, *J. Am. Chem. Soc.*, 2020, **142**, 20962–20967.

8 L. Chen, M.-J. Zhang, S.-Y. Zhang, L. Shi, Y.-M. Yang, Z. Liu, X.-J. Ju, R. Xie, W. Wang and L.-Y. Chu, *ACS Appl. Mater. Interfaces*, 2020, **12**, 35120–35131.

9 S. Sánchez, L. Soler and J. Katuri, *Angew. Chem., Int. Ed.*, 2015, **54**, 1414–1444.

10 Y. Ying, A. M. Pourrahimi, Z. Sofer, S. Matějková and M. Pumera, *ACS Nano*, 2019, **13**, 11477–11487.

11 H. Huang, J. Li, M. Yuan, H. Yang, Y. Zhao, Y. Ying and S. Wang, *Angew. Chem., Int. Ed.*, 2022, **61**, e202211163.

12 T. Xu, F. Soto, W. Gao, R. Dong, V. Garcia-Gradilla, E. Magaña, X. Zhang and J. Wang, *J. Am. Chem. Soc.*, 2015, **137**, 2163–2166.

13 F. Ji, D. Jin, B. Wang and L. Zhang, *ACS Nano*, 2020, **14**, 6990–6998.

14 Z. Ye, Y. Sun, H. Zhang, B. Song and B. Dong, *Nanoscale*, 2017, **9**, 18516–18522.

15 D. P. Singh, W. E. Uspal, M. N. Popescu, L. G. Wilson and P. Fischer, *Adv. Funct. Mater.*, 2018, **28**, 1706660.

16 J. G. Lee, A. M. Brooks, W. A. Shelton, K. J. M. Bishop and B. Bharti, *Nat. Commun.*, 2019, **10**, 2575.

17 Y. Dou, C. A. Cartier, W. Fei, S. Pandey, S. Razavi, I. Kretzschmar and K. J. M. Bishop, *Langmuir*, 2016, **32**, 13167–13173.

18 L. Ren, N. Nama, J. M. McNeill, F. Soto, Z. Yan, W. Liu, W. Wang, J. Wang and T. E. Mallouk, *Sci. Adv.*, 2019, **5**, eaax3084.

19 W. Liu, X. Chen, X. Ding, Q. Long, X. Lu, Q. Wang and Z. Gu, *Nanoscale Horiz.*, 2021, **6**, 238–244.

20 M. Chen, Z. Lin, M. Xuan, X. Lin, M. Yang, L. Dai and Q. He, *Angew. Chem., Int. Ed.*, 2021, **60**, 16674–16679.

21 S. Zheng, Y. Wang, S. Pan, E. Ma, S. Jin, M. Jiao, W. Wang, J. Li, K. Xu and H. Wang, *Adv. Funct. Mater.*, 2021, **31**, 2100936.

22 C. Chen, F. Mou, L. Xu, S. Wang, J. Guan, Z. Feng, Q. Wang, L. Kong, W. Li, J. Wang and Q. Zhang, *Adv. Mater.*, 2017, **29**, 1603374.

23 J. Palacci, S. Sacanna, A. P. Steinberg, D. J. Pine and P. M. Chaikin, *Science*, 2013, **339**, 936–940.

24 G. Zhu, M. Hannel, R. Sha, F. Zhou, M. Y. B. Zion, Y. Zhang, K. Bishop, D. Grier, N. Seeman and P. Chaikin, *Proc. Natl. Acad. Sci. U. S. A.*, 2021, **118**, e2023508118.

25 Y. Xing, S. Tang, X. Du, T. Xu and X. Zhang, *Nano Res.*, 2021, **14**, 654–659.

26 L. Xu, F. Mou, H. Gong, M. Luo and J. Guan, *Chem. Soc. Rev.*, 2017, **46**, 6905–6926.

27 R. María Hormigos, B. Jurado Sánchez and A. Escarpa, *Angew. Chem., Int. Ed.*, 2019, **58**, 3128–3132.

28 K. Villa and M. Pumera, *Chem. Soc. Rev.*, 2019, **48**, 4966–4978.

29 T. Xu, W. Gao, L.-P. Xu, X. Zhang and S. Wang, *Adv. Mater.*, 2017, **29**, 1603250.

30 C. Liu, J. Huang, T. Xu and X. Zhang, *Microchim. Acta*, 2022, **189**, 116.

31 X. Zhou, Z. Li, L. Tan, Y. Zhang and Y. Jiao, *ACS Appl. Mater. Interfaces*, 2020, **12**, 23134–23144.

32 Y. Ying, J. Plutnar and M. Pumera, *Small*, 2021, **17**, 2100294.

33 B. Khezri and M. Pumera, *Adv. Mater.*, 2019, **31**, 1806530.

34 A. Terzopoulou, J. D. Nicholas, X.-Z. Chen, B. J. Nelson, S. Pané and J. Puigmartí-Luis, *Chem. Rev.*, 2020, **120**, 11175–11193.

35 B. Wang, A. P. Côté, H. Furukawa, M. O'Keeffe and O. M. Yaghi, *Nature*, 2008, **453**, 207–211.

36 K. S. Park, Z. Ni, A. P. Côté, J. Y. Choi, R. Huang, F. J. Uribe-Romo, H. K. Chae, M. O'Keeffe and O. M. Yaghi, *Proc. Natl. Acad. Sci. U. S. A.*, 2006, **103**, 10186–10191.

37 R. Banerjee, A. Phan, B. Wang, C. Knobler, H. Furukawa, M. O'Keeffe and O. M. Yaghi, *Science*, 2008, **319**, 939–943.

38 A.-N. Au-Duong and C.-K. Lee, *Mater. Sci. Eng., C*, 2017, **76**, 477–482.

39 J. Wang, Y. Wang, Y. Zhang, A. Uliana, J. Zhu, J. Liu and B. Van der Bruggen, *ACS Appl. Mater. Interfaces*, 2016, **8**, 25508–25519.

40 Z. Song, Y. Wu, Q. Cao, H. Wang, X. Wang and H. Han, *Adv. Funct. Mater.*, 2018, **28**, 1800011.

41 M. Taheri, T. G. Enge and T. Tsuzuki, *Mater. Today Chem.*, 2020, **16**, 100231.

42 H. Zhang, M. Zhao, Y. Yang and Y. S. Lin, *Microporous Mesoporous Mater.*, 2019, **288**, 109568.

43 M. Taheri and T. Tsuzuki, *ACS Mater. Lett.*, 2021, **3**, 255–260.

44 M. Taheri, D. Ashok, T. Sen, T. G. Enge, N. K. Verma, A. Tricoli, A. Lowe, D. R. Nisbet and T. Tsuzuki, *Chem. Eng. J.*, 2021, **413**, 127511.

45 Y.-W. Wang, A. Cao, Y. Jiang, X. Zhang, J.-H. Liu, Y. Liu and H. Wang, *ACS Appl. Mater. Interfaces*, 2014, **6**, 2791–2798.

46 J. Tan, D. Wang, H. Cao, Y. Qiao, H. Zhu and X. Liu, *ACS Appl. Mater. Interfaces*, 2018, **10**, 42018–42029.

47 Z. Zha, Z. Deng, Y. Li, C. Li, J. Wang, S. Wang, E. Qu and Z. Dai, *Nanoscale*, 2013, **5**, 4462–4467.

48 Y.-D. Zhu, S.-P. Chen, H. Zhao, Y. Yang, X.-Q. Chen, J. Sun, H.-S. Fan and X.-D. Zhang, *ACS Appl. Mater. Interfaces*, 2016, **8**, 34209–34217.

49 D. K. L. Harijan, V. Chandra, T. Yoon and K. S. Kim, *J. Hazard. Mater.*, 2018, **344**, 576–584.

50 Y. Zhou, Y. Hu, W. Sun, S. Lu, C. Cai, C. Peng, J. Yu, R. Popovtzer, M. Shen and X. Shi, *Biomacromolecules*, 2018, **19**, 2034–2042.

51 M. Rivero, J. Hu, D. Jaque, M. Cañete, J. Sánchez-Marcos and A. Muñoz-Bonilla, *J. Phys. Chem. C*, 2018, **122**, 16389–16396.

52 R. K. Manna, O. E. Shklyaev, J. Kauffman, B. Tansi, A. Sen and A. C. Balazs, *ACS Appl. Mater. Interfaces*, 2019, **11**, 18004–18012.

53 W. Liu, W. Wang, X. Dong and Y. Sun, *ACS Appl. Mater. Interfaces*, 2020, **12**, 12618–12628.

54 C. Lozano, B. ten Hagen, H. Löwen and C. Bechinger, *Nat. Commun.*, 2016, **7**, 12828.

55 B. Dai, J. Wang, Z. Xiong, X. Zhan, W. Dai, C.-C. Li, S.-P. Feng and J. Tang, *Nat. Nanotechnol.*, 2016, **11**, 1087–1092.

56 R. Li, T. Chen and X. Pan, *ACS Nano*, 2021, **15**, 3808–3848.